Check for updates

ADVANCED FUNCTIONAL MATERIALS
www.afm-journal.de

Composites from Self-Assembled Protein Nanofibrils and Liquid Metal Gallium

Li Liu, Md. Arifur Rahim, Tianchen Li, Mohamed Kilani, Yilin He, Zeyu Shao, Jiewei Zheng, Chen Wang, Mahroo Baharfar, Shih-Hao Chiu, Jake Ireland, Timothy L. Sorenson, Aditya Rawal, Maedehsadat Mousavi, Mohammad B. Ghasemian, Chengchen Zhang, Jianbo Tang, Edgar H. H. Wong, Jin Zhang, Francois-Marie Allioux, Kourosh Kalantar-Zadeh,* and Yi Shen**

Gallium (Ga), a low-melting-point liquid metal with soft, metallic, and biocompatible properties, offers many possibilities. However, the potential of composites that integrate Ga with biomacromolecules, combining their biocompatibility, elasticity, and conductivity, has not been thoroughly explored, which is a gap for advancing these composites in various applications. In parallel and independently, protein self-assembled l.,;3bhnanofibrils have attracted great interest as building blocks for functional biomaterials. Here, composites of Ga droplets and nanofibrils are presented, self-assembled from plant proteins of soy protein isolate (SPI). It is evidenced that in these composites self-assembled SPI nanofibrils can effectively reduce the oxidation of Ga droplets. It is observed that the composites of β-sheet nanofibrils and Ga droplets offer mechanical properties similar to only fibrils-based films. Films of 32 wt% Ga in SPI showed enhanced electrical conductivity and well-structured nanofibrils with multifunctional potential in gas-sensing and electronically controlled antibacterial applications. It is illustrated that the 32 wt% Ga in SPI composite offered the best sensing performance for a diatomic molecule, CO, and electro-stimulation of this composite effectively reduced bacterial growth. The Ga in SPI composite, combining the advantages of protein nanofibrils and Ga droplets, offers great potential in future biomedical applications.

1. Introduction

Liquid metals (LMs), as emerging functional soft materials, present unique advantages, such as high fluidity for processibility,[1] and excellent electrical conductivity.[2] These characteristics have led to widespread interest in their applications in diverse fields, including catalysis,[3] sensing,[4] soft and flexible electronics,[5] and bioengineering.[6] Among the LMs groups, gallium (Ga) and its alloys have been extensively studied in biomaterial and sensing-related areas due to Ga low melting point (29.8 °C),[7] low toxicity,[6b] stimuli-responsive properties,[8] and ease of preparation.[9] In this regard, a key research focus is integrating Ga droplets with polymers and organic materials to create functional composites[2c,10] for applications in cell growth,[11] electronic skin,[12] sensors,[4] and drug delivery.[13] The softness and low melting point of Ga allow for low-temperature processes that permit the facile breakdown of the

L. Liu, M. A. Rahim, T. Li, C. Wang, S.-H. Chiu, T. L. Sorenson, M. B. Ghasemian, F.-M. Allioux, K. Kalantar-Zadeh, Y. Shen
School of Chemical and Biomolecular Engineering
The University of Sydney
Sydney, NSW 2006, Australia
E-mail: f.allioux@sydney.edu.au; kourosh.kalantarzadeh@sydney.edu.au; yi.shen@sydney.edu.au

L. Liu, M. A. Rahim, M. Kilani, Z. Shao, J. Zheng, M. Baharfar, S.-H. Chiu, J. Ireland, M. Mousavi, M. B. Ghasemian, J. Tang, E. H. H. Wong, F.-M. Allioux, K. Kalantar-Zadeh
School of Chemical Engineering
University of New South Wales (UNSW)
Sydney, NSW 2052, Australia

M. A. Rahim
Department of Chemical and Biological Engineering
Monash University
Clayton, VIC 3800, Australia

Y. He, J. Zhang
School of Mechanical and Manufacturing Engineering
University of New South Wales (UNSW)
Sydney, NSW 2052, Australia

The ORCID identification number(s) for the author(s) of this article can be found under https://doi.org/10.1002/adfm.202405918

© 2024 The Author(s). Advanced Functional Materials published by Wiley-VCH GmbH. This is an open access article under the terms of the Creative Commons Attribution License, which permits use, distribution and reproduction in any medium, provided the original work is properly cited.

DOI: 10.1002/adfm.202405918

16163028, 2024, 45, Downloaded from https://advanced.onlinelibrary.wiley.com/doi/10.1002/adfm.202405918 by University Of Southampton, Wiley Online Library on [23/07/2025]. See the Terms and Conditions (https://onlinelibrary.wiley.com/terms-and-conditions) on Wiley Online Library for rules of use; OA articles are governed by the applicable Creative Commons License

Ga-based LM into small droplets for incorporation within composites.[14] Avoiding harsh environments for processing composites is especially critical for integrating biomacromolecules in such composites.[15] However, the properties of composite materials that combine Ga with biomacromolecules, such as carbohydrates, proteins, and lipids, remain relatively underexplored. In one example of such a possibility, composites of Ga droplets with cellulose have been investigated for flexible and deformable electronics.[16] In another study, biocompatible and biodegradable gluten-LMs composites have been demonstrated for protein-based self-healable electronic skin.[17] In this regard, compositing nature-sourced biomaterials with Ga can be of potential interest and warrant specific attention.

Biomaterials derived from natural sources, particularly proteins and peptides, are of research interest,[18] especially in the areas of sensing[19] and also antibacterial behavior[20] due to their biocompatibility and eco-friendly nature.[18,21] Among these biomaterials, amyloid fibrils, although considered as one of the main causes of neurodegenerative diseases, have also been considered in a variety of applications due to their interesting structures. More recent research has revealed that a wide range of non-pathological proteins can self-assemble into β-sheet rich nanofibrillar structures, similar to amyloid fibrils, that can impart materials with enhanced continuity, tensile strength, and stability.[22] Thus, the potential of using protein nanofibrils as building blocks in functional materials has attracted great attention for different applications such as in cell growth scaffolds,[23] biosensors,[24] and energy conversion.[25] Many protocols have been developed for manufacturing nanofibrils from food proteins including plant-based proteins,[26] which are widely available from low-cost sources. To further expand their functionalities, nanofibrils-based composites have been developed by incorporating inorganic particles, including gold,[27] carbon,[28] graphene,[29] and silver particles[30] to produce hydrogels and aerogels.[31] Despite previous successful demonstrations of nanofibrils-inorganic composites with intriguing properties, the research and applications of these composites have remained limited. This limitation is primarily due to the non-biocompatibility of these composite materials caused by their inorganic nature such as carbon-based constructs[28] and the non-biocompatible additives during their synthesis processes.[29,31c,32] Furthermore, in most studies, individual inorganic particles are limited to a narrow functionality.[30] Therefore, it is challenging, but desirable, to create novel hybrid material combinations with ease of preparation, biocompatibility, and diverse functionalities.

Due to the liquid nature of Ga, nanofibrils-Ga composites can be prepared using a simple one-step process of sonication without introducing severely toxic additives. Moreover, Ga droplets are known for their high electrical conductivity, responsivity to electromagnetic waves,[33] and biocompatibility compared to traditional solid nanoparticles including gold and carbon nanomaterials.[13a] Gallium has been extensively studied for near-infrared photothermal therapy,[34] bioimaging,[35] and biosensors,[4] and as such, the combination of Ga and nanofibrils can possibly offer multifunctional capabilities that are desirable for diverse application areas.

Herein, we develop a composite film that integrates Ga droplets with plant protein nanofibrils. The well-structured nanofibrils form around Ga droplets via an in situ self-assembly of plant protein isolate. We show that the mix of nanofibrils and Ga droplets creates composites that are both conductive and possess robust mechanical properties. Our results further suggest that the self-assembled nanofibrils reduce the oxidation of embedded Ga droplets, sintering them to conductive patterns. We hypothesize that self-assembled nanofibrils-Ga composites can be sensitive and selective to specific gas species due to their particular alignments within nanofibrils.[36] The enhanced electron transfer-ability of the composite enhances the gas-sensing responsivity and stability compared to only Ga droplets or only nanofibrils. It is also conceivable that electrical conductivity with antibacterial Ga ions can help in killing bacteria under the influence of an applied voltage in such composites. As such, we demonstrate the electrical conductivity from Ga droplets endows the protein-based film with electrical stimulation ability, offering antibacterial properties.

2. Results and Discussion

2.1. Preparation and Characterization of the SPI-Ga Films

Soy protein isolate (SPI), derived from soybeans as a byproduct, is an easily accessible, cost-effective, and sustainable plant-based protein source.[37] Thus, SPI (Figure S1a, Supporting Information) is chosen as the model plant-based protein for nanofibril formation and synthesis of the SPI self-assembled nanofibril-Ga composite(SPI-Ga composite).

In this study, we synthesize SPI-Ga composite films by adopting in situ self-assembly of SPI nanofibrils with an aqueous dispersion of liquid Ga droplets. The preparation of the SPI-Ga composite films is schematically shown in **Figure 1a**, and the details are provided in the Experimental Section. Based on previous studies,[26a] we dissolve and denature SPI through sonication in a 30% acetic acid aqueous solution at 90 °C. Sonication with elevated temperature in acetic acid is applied in order to disrupt large SPI into smaller particles and denature the SPI into soluble isolate.[38] The SPI unfold and partially hydrolyze, making them more accessible for forming new intermolecular interactions.[39] This turns the white insoluble soy protein solution (Figure S1b, Supporting Information) into a translucent aqueous solution (Figure S1c, Supporting Information). It should be noted that we find lowering the temperature below 90 °C during denaturation, resulting in thinning of the nanofibrils and weak mechanical properties (Figure S2, Supporting Information). As the temperature is gradually lowered, the translucent solution gels up, indicating the formation of a dense fibrillar network, consistent with a previous study.[26a] Transmission electron microscopy (TEM) imaging (Figure S3, Supporting Information) of self-assembled SPI presents a similar morphology to previously reported SPI nanofibrils in pH of ≈2–3.[26a,40] As shown in

A. Rawal
Nuclear Magnetic Resonance Facility
Mark Wainwright Analytical Center
The University of New South Wales
Sydney, NSW 2052, Australia
C. Zhang
School of Electronics and Computer Science (ECS)
The University of Southampton
Southampton SO17 1BJ, UK

© 2024 The Author(s). Advanced Functional Materials published by Wiley-VCH GmbH

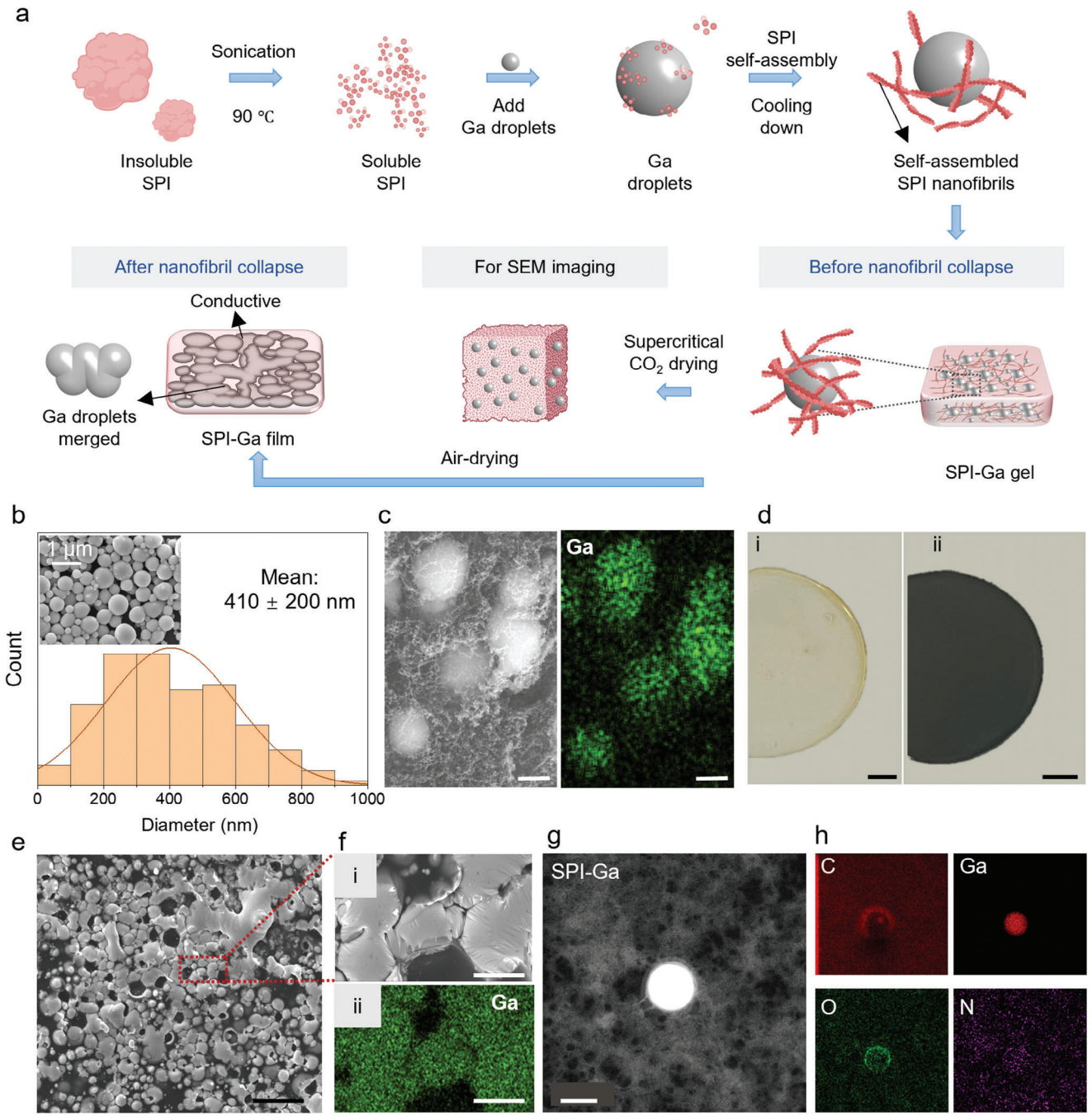

Figure 1. Synthesis and characterization of SPI-Ga films made of nanofibrils. a) Schematics for SPI-Ga film synthesis. b) Size distribution and the corresponding SEM image of Ga droplets sonicated in ethanol for 30 min. Scale bar: 1 μm. c) SEM and EDS images of SPI-Ga hydrogel prepared through supercritical CO_2 drying. Scale bar: 500 nm. d) Photos of i) self-assembled SPI film and ii) SPI-Ga 32 wt% film. Scale bar: 1 cm. e) SEM image of the bottom surface of SPI-Ga 32 wt% film and f) i) SEM image of the enlarged bottom surface of SPI-Ga 32 wt% film with ii) corresponding EDS image showing Ga droplets merged in the SPI-Ga 32 wt% film. Scale bar: e) 20 μm, f) 5 μm. g) STEM and h) STEM-EDS images of SPI-Ga 32 wt% composite. Scale bar: 100 nm.

Figure S3 (Supporting Information) if the solution is diluted to a low concentration before cooling, almost no nanofibril forms. The solutions diluted during and after the cooling process show the growth of nanofibrils from short oligomers to longer structures.

To prepare the self-assembled SPI-Ga composite films (SPI-Ga films), liquid Ga droplets are synthesized via sonication to obtain droplets with an average size of 410 ± 200 nm (Figure 1b) and then introduce them into the translucent SPI solution for further sonication. Sonication not only helps to homogenize the

© 2024 The Author(s). Advanced Functional Materials published by Wiley-VCH GmbH

16163028, 2024, 45, Downloaded from https://advanced.onlinelibrary.wiley.com/doi/10.1002/adfm.202405918 by University Of Southampton, Wiley Online Library on [23/07/2025]. See the Terms and Conditions (https://onlinelibrary.wiley.com/terms-and-conditions) on Wiley Online Library for rules of use; OA articles are governed by the applicable Creative Commons License

dispersion of Ga droplets in the SPI solution but also exposes the fresh liquid Ga surfaces to cavitation. This process facilitates the interaction of Ga droplets with the functional groups of proteins, such as amine and carboxyl groups, which have been reported to self-assemble around the droplets' surface.[41] Upon reducing the temperature, the soluble SPI self-assembles into nanofibrils with incorporated Ga droplets, forming a self-supporting hydrogel (Figure S4, Supporting Information). To confirm the formation of nanofibrils, the obtained SPI-Ga hydrogel is prepared through supercritical CO_2 drying (see Experimental Section) to maintain the nanofibrils structures. The scanning electron microscopy (SEM) imaging shows that SPI-Ga hydrogel exhibits a densely packed nanofibrils network (Figure 1c), indicating the minimum visual influence of Ga droplets on the nanofibrils formation.

Following three days of air-drying, the nanofibrils structure is observed to collapse and compact around Ga droplets, resulting in a self-standing composite film (Figure 1d). The SEM images of the bottom surface of SPI-Ga film contain a high concentration of Ga droplets (Figure 1e), and the Ga droplets are merged into connected patterns (Figure 1f), which converts the film from non-conductive to conductive.

To obtain insight into the SPI-Ga droplets interfacial interaction, we measure the size of Ga droplets after the mixing process to confirm the absorption of SPI and self-assembled SPI on Ga droplets. The dynamic light scattering (DLS) assessments show that the initial hydrodynamic sizes of Ga droplets are 387 ± 176 nm (Figure S5, Supporting Information – also in good agreement with Figure 1b). Following co-culture with native SPI and self-assembled SPI, the sizes increase to 533 ± 105 and 659 ± 326 nm, respectively, indicating the formation of native SPI and self-assembled SPI on the surface of the Ga droplets. Besides, the TEM of SPI-Ga hydrogel after dilution and the SEM images of SPI-Ga hydrogel after critical point drying also indicate the formation of self-assembled SPI on the surface of Ga droplets (Figures S3 and S6, Supporting Information). Furthermore, the Scanning TEM (STEM) image and corresponding energy-dispersive X-ray spectroscopy (EDS, Figure 1g) confirm the formation of self-assembled SPI around Ga droplets, compared with Ga droplets only (Figure S7, Supporting Information). This helps to reduce the oxidation level of Ga droplets which is characterized and discussed in Section 2.2.

X-ray photoelectron spectroscopy (XPS) analysis on the bottom surface of Ga droplets, SPI films, and SPI-Ga films shows that the peaks of Ga with and without nanofibrils are identical without shifting, implying no chemical bonding formed (Figures S8 and S9, Supporting Information). Meanwhile, the contact angle of Ga droplets on self-assembled SPI-coated glass in acetic acid is above 110° (>90°), indicating dewetting interactions (Figure S10, Supporting Information). Besides, the zeta (ζ) potential of Ga droplets shifts from a negative to a positive value after co-culturing with native SPI or self-assembled SPI in acetic acid (Figure S11, Supporting Information). These results indicate that electrostatic interactions are present between Ga droplets and self-assembled SPI, which can be one of the reasons for the self-assembled SPI on the droplets' surface.

Therefore, the mechanism of SPI-Ga composite formation is proposed as follows: sonicating insoluble native SPI at 90 °C creates a highly dissolved concentration of protein in the solution. After the addition of Ga droplets, the fresh surface of liquid Ga droplets is also exposed by cavitation via sonication, facilitating the affinity of SPI onto the surface with a very thin self-limiting oxide of Ga. Subsequently, lowering the temperature after sonication promotes SPI self-assembling into fibrils with Ga incorporated, leading to the formation of the composite material.

The uniformity of the film is closely related to the undisturbed self-assembly process, which can be ensured by optimizing Ga droplet size. When the size of the droplets is reduced to 195 ± 101 nm (Figure S12, Supporting Information – when the sonication duration is increased to 60 min), the Ga droplets react quickly with acetic acid at 90 °C, thus producing excessive hydrogen gas to form bubbles and thicker surface oxide, which hinders the formation of the film (Figure S13, Supporting Information). Besides, simply mixing Ga droplets with SPI in solution without inducing SPI self-assembly into nanofibrils results in the formation of cracked films (Figure S14, Supporting Information). These results imply the vital role of self-assembled nanofibrils in the formation of self-standing composite films and importance of the optimal droplets dimensions.

2.2. Properties of the SPI-Ga Films

By incorporating various weight ratios of Ga droplets into the composite, we investigate the impact of Ga droplet concentration on the structure of the composite films. **Figure 2**a illustrates the morphology of the SPI-Ga films with increasing the concentration of Ga droplets. When the weight of self-assembled SPI is kept constant and the Ga droplet concentration increases up to 32 wt%, the film maintains a continuous and homogeneous morphology. However, when the Ga droplet concentration reaches ≈42 wt%, the film begins to crack. This is mainly attributed to the increased number of Ga droplets reacting with acetic acid, which produces more bubbles during the process that disrupt the uniform fibril formation. On the other hand, reducing the mass of SPI results in a thinner and less homogeneous film. Therefore, for further research, five films displaying optimal integrity and uniformity, as marked in the red dashed box in Figure 2a, are selected. These films represent different Ga/self-assembled SPI ratios, with Ga weight ratios of 0, 2, 8, 20, and 32 wt%.

To quantify the influence of Ga droplets on SPI film's transparency, we obtain ultraviolet–visible (UV–Vis) transmittance spectra of the composite films. Figure 2b shows that the concentration of Ga droplets significantly influences the transparency of the films. Films with Ga droplet ratios below 8 wt% maintain high transparency, exhibiting transmittance above 80%. However, films with ratios exceeding 20 wt% show a significant decrease in transmittance, blocking nearly all light transmissions.

We further investigate the influence of Ga droplets on protein self-assembly, using attenuated total reflectance Fourier-transform infrared spectroscopy (ATR-FTIR) (Figure 2c). The effect of Ga droplets on protein secondary structure can be characterized by the second derivative of the amide I band of protein (1700–1600 cm^{-1}) in the IR spectrum.[42] As shown in Figure S15 (Supporting Information), the ATR-FTIR spectrum of the SPI film exhibits a higher amount of β-sheets structure compared to the native SPI, suggesting successful induction of protein self-assembly and the formation of β-sheets-rich nanofibrils during the synthesis process. Interestingly, the addition of 2 and 8 wt%

© 2024 The Author(s). Advanced Functional Materials published by Wiley-VCH GmbH

16163028, 2024, 45, Downloaded from https://advanced.onlinelibrary.wiley.com/doi/10.1002/adfm.202405918 by University Of Southampton, Wiley Online Library on [23/07/2025]. See the Terms and Conditions (https://onlinelibrary.wiley.com/terms-and-conditions) on Wiley Online Library for rules of use; OA articles are governed by the applicable Creative Commons License

16163028, 2024, 45, Downloaded from https://advanced.onlinelibrary.wiley.com/doi/10.1002/adfm.202405918 by University Of Southampton, Wiley Online Library on [23/07/2025]. See the Terms and Conditions (https://onlinelibrary.wiley.com/terms-and-conditions) on Wiley Online Library for rules of use; OA articles are governed by the applicable Creative Commons License

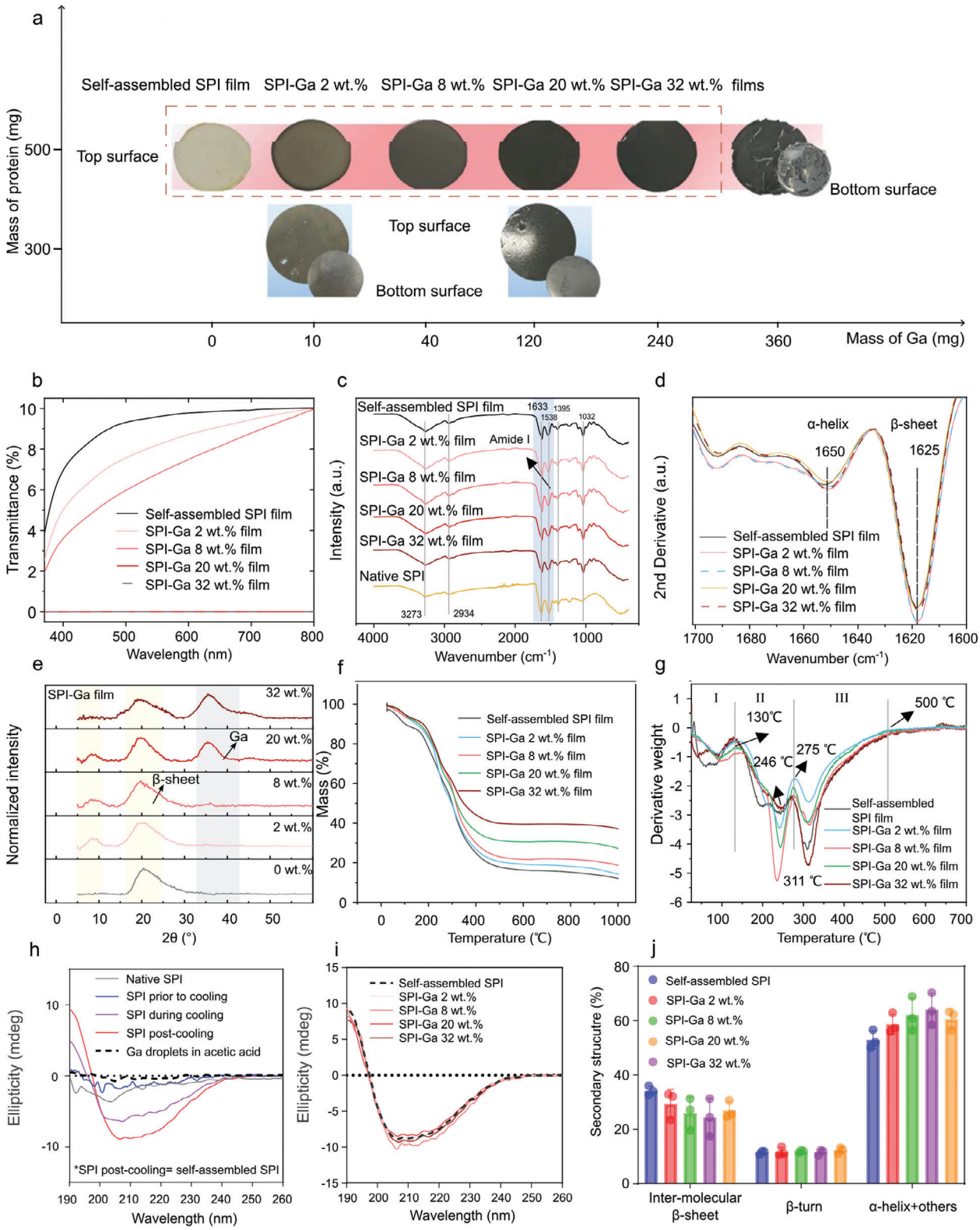

Figure 2. Structural characterization of SPI-Ga composite films. a) Impact of different masses of Ga and native SPI on the morphology of the films. b–g) Characterization of self-assembled SPI and SPI-Ga films with a different Ga mass ratio: (b) UV–vis spectra; c) FTIR and d) Secondary derivative of FTIR (1600–1700 cm^{-1}); e) XRD; f) TGA; g) DTG curves. h) CD spectra of native SPI in different stages after sonication. i) Representative data of CD spectra SPI-Ga samples. j) Quantitative analysis of protein secondary structures of self-assembled SPI and SPI-Ga composites using BeStSel ($n = 3$, ns. $p > 0.05$).

 © 2024 The Author(s). Advanced Functional Materials published by Wiley-VCH GmbH

Ga droplets to the SPI-Ga films results in a slightly higher content of β-sheets (peak at 1625 cm^{-1}) while the SPI-Ga 32 wt% film displays a similar β-sheets content to the SPI film (Figure 2d). These results indicate that the addition of Ga droplets does not disturb the formation of intact β-sheet structure.

X-ray diffraction analysis (XRD) is employed to further investigate the influence of Ga droplets on the secondary structure of SPI films (Figure 2e). In the self-assembled SPI film, a typical peak is observed at 2θ of 19.19° (d-spacing value of ≈4.7 Å), representing the inter-strand spacing of β-sheet structures.[38] For SPI-Ga films, the peaks corresponding to β-sheets do not show significant changes compared with that of the self-assembled SPI film, indicating a negligible influence of Ga droplets on protein secondary structure. Additionally, the characteristic broad features observed in the XRD patterns of the SPI-Ga films are attributed to Ga in the liquid state,[43] indicating that the Ga droplets remain in the liquid state within the composite. The liquid phase of Ga is observed at room temperature possibly due to the supercooling of Ga droplets within the composites.[44]

It has been reported that the presence of nanofibrils can improve materials' thermal stability due to the increased hydrogen bonding and hydrophobic interactions.[36] Thus, we further investigate whether the incorporation of Ga affects the thermal gravimetric analysis (TGA) performance of the films (Figure 2f). As the temperature increases, the SPI burns out and the water evaporates from the films, while Ga with a boiling point of 2400 °C,[45] remains. Notedly, the weight loss of SPI film and SPI-Ga films presents different trends, as shown in the derivative thermogravimetric (DTG) curves (Figure 2g). Generally, the temperature stages of weight loss in the films are 0–130 °C due to water evaporation; 130–275 °C from glycerol evaporation and chemical bond breaks; 275–500 °C, where the main peptide chain breaks, involving C—O, C—C, and C—N bonds, resulting in the largest weight loss. The 10% weight remaining at the end of TGA for SPI film is attributed to char residue formed in the N_2 atmosphere (Figure S16, Supporting Information), which is consistent with other research studies.[46] Specifically, the SPI film exhibits two peaks at ≈246 and 311 °C, corresponding to the breaking of the hydrogen bond and the main peptide chain of protein, respectively. The degradation peaks of the SPI-Ga films are similar to those of the SPI film ≈245 °C. These results suggest that the thermal stability of the SPI-Ga films shows no significant difference from that of the SPI film, indicating nanofibrils formed well in the SPI-Ga films. The differential scanning calorimetry (DSC) analysis (Figure S17, Supporting Information) of the SPI and SPI-Ga films shows three peaks, at 80, 250, and 320 °C, present across all samples, which are associated with the loss of moisture, the breakdown of intermolecular interactions, and the breakdown of the primary structure, respectively.[47] Additionally, the DSC analysis of SPI-Ga samples presents a small sign yet distinct phase transition event at ≈30 °C corresponding to Ga.

The circular dichroism (CD) spectra of native SPI samples in different stages after sonication are also obtained and shown in Figure 2h. The ellipticity of SPI post-cooling at 218 nm distinctly increases compared to native SPI before sonication and prior to cooling, indicating the formation of β-sheets after sonication during cooling (Figure S18, Supporting Information). The ellipticity of the SPI-Ga composite with different Ga concentrations at 218 nm does not show a significant decrease (Figure 2i,j; Figure S19, Supporting Information), indicating that Ga droplets at concentrations up to 32 wt% do not influence the β-sheets formation. Moreover, the 1H NMR analysis of native SPI, self-assembled SPI, and SPI-Ga 32 wt% strongly complements the other analyses, confirming the formation and stability of the nanofibrils in the SPI-Ga composites (Figures S20 and S21, Supporting Information). Taking all the results collectively, the formation of self-assembled SPI with beta-sheets is not negatively influenced by a certain concentration of Ga droplets.

The presence of a β-sheet-rich secondary structure in the composite film suggests favorable mechanical properties for the formation of free-standing films.[21a] Therefore, we further investigate the mechanical properties and electrical conductivity of the SPI-Ga film to determine if a desired balance between the mechanical strength from the nanofibrils and the electrical conductivity from Ga can be achieved. We perform tensile tests on SPI film and SPI-Ga films with three replicates for each sample group (Figure S22, Supporting Information). The representative data for each group are presented in **Figure 3a**. The results show no statistically significant differences in Young's modulus (Figure 3b), ultimate tensile strength (Figure S23a, Supporting Information), and elongation at break (Figure S23b, Supporting Information) for each group. These outcomes indicate that the mechanical properties resulting from the formation of self-assembled SPI are not impacted by the addition of Ga droplets. We then study the electrical conductivity of the SPI-Ga films. After three days of air drying, the conductivity of SPI-Ga films is measured. As the concentration of Ga droplets increases, the electrical conductivity of the SPI-Ga composite changes from non-conductive (for the SPI sample) to $3.20 \pm 0.21 \times 10^{-2}$ S m^{-1} (for the SPI-Ga 32 wt% sample) (Figure 3c). The conductivity of film made only of Ga droplets is $1.12 \pm 0.03 \times 10^{-5}$ S m^{-1} as a reference. The SEM images of SPI films with different Ga concentrations reveal that with increasing Ga loading, the Ga droplets merge into continuous and homogeneous conductive pathways across the SPI-Ga composites (Figure S24, Supporting Information). The Ga concentration is larger at the bottom of the composite due to the higher density of Ga over SPI. After solvent evaporation and the nanofibrils collapse, the bottom surface is rich in merged Ga (Figure 1e,f), while the top surface (Figure S25, Supporting Information) presents isolated Ga droplets. This increase represents a three-order-of-magnitude enhancement in electrical conductivity compared to the Ga droplets only, which also effectively turns the originally non-conductive SPI film conductive.

To elucidate the mechanism behind the observed electrical conductivity, we employ XPS to investigate the influence of SPI on the Ga oxidation state. Compared with Ga droplets, the Ga droplets embedded in the SPI film show less oxidation. Figure 3d,e presents the Ga 3d photoelectron spectra of Ga droplets and SPI-Ga 32 wt% film, respectively. The XPS patterns clearly show the presence of Ga in the metallic state and Ga oxide layer since peaks corresponding to Ga^0, and Ga^{3+} (colored as blue, brown, and red, respectively, in Figure 3d,e) are observed. However, while the same peaks are also observed for SPI-Ga 32 wt% film, the film shows a much more intense peak of Ga° compared to the Ga droplets only. To further strengthen this observation, XPS depth profiling analysis is also performed. For the Ga droplets sample, a strong signal is observed ≈20 eV within the first 300 nm from the surface in the depth profiling

© 2024 The Author(s). Advanced Functional Materials published by Wiley-VCH GmbH

16163028, 2024, 45, Downloaded from https://advanced.onlinelibrary.wiley.com/doi/10.1002/adfm.202405918 by University Of Southampton, Wiley Online Library on [23/07/2025]. See the Terms and Conditions (https://onlinelibrary.wiley.com/terms-and-conditions) on Wiley Online Library for rules of use; OA articles are governed by the applicable Creative Commons License

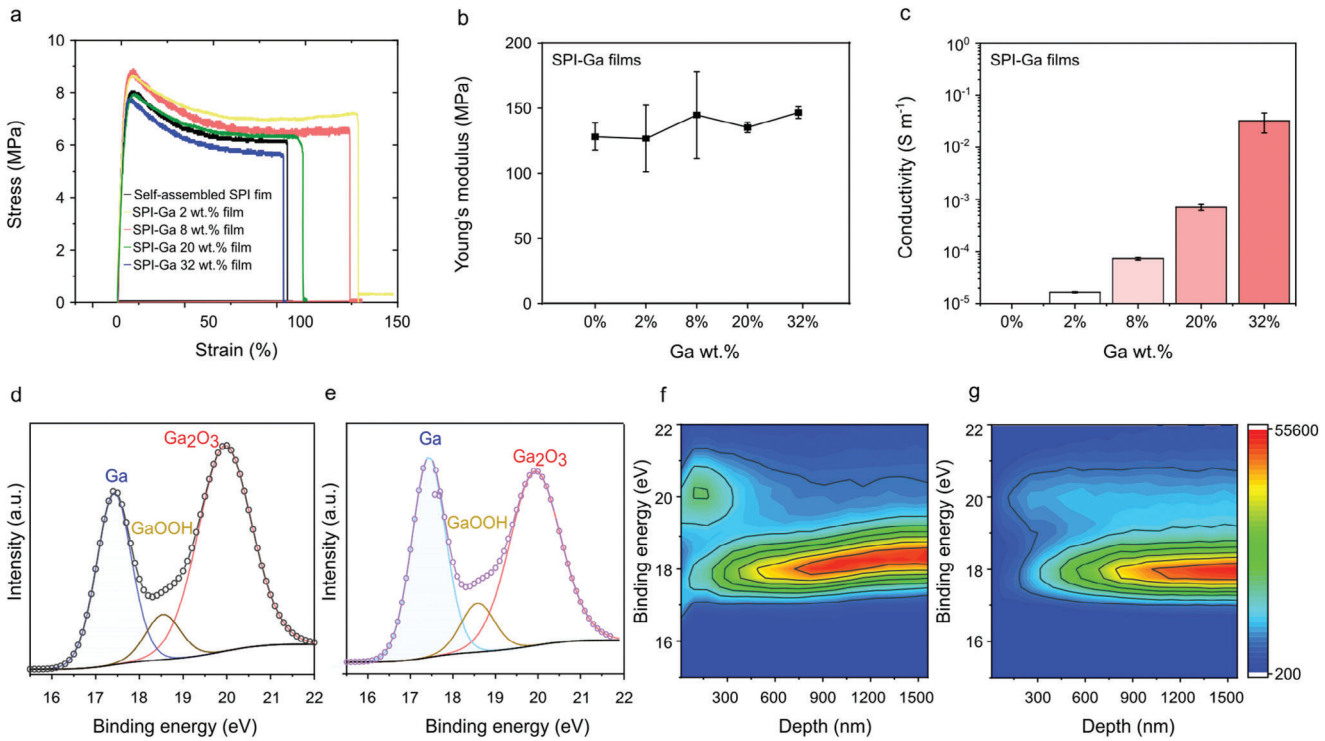

Figure 3. Physical and chemical properties of the SPI-Ga composite films. a,b) Mechanical properties of the SPI-Ga films: (a) The tensile test and (b) Young's modulus of SPI films and SPI-Ga films ($n = 3$, ns. $P > 0.05$). c) The electrical conductivity of SPI film and SPI-Ga films. d–g) XPS analyses of Ga droplets: XPS spectra of Ga 3d on (d) Ga droplets only and (e) Ga droplets in SPI-Ga 32 wt% film (bottom surface); XPS depth profiles of Ga 3d on (f) Ga droplets only and (g) Ga droplets in SPI-Ga 32 wt% film (bottom surface).

map, which corresponds to the Ga oxide (Ga^{3+}) layer (Figure 3f). However, the signal at 20 eV for Ga droplets in SPI-Ga film is much weaker (Figure 3g). Besides, the distribution of signal intensity ≈18.5 eV is more confined (Figure 3g) compared to Ga droplets only (Figure 3f), indicating that the Ga droplets encapsulated in SPI film are less oxidized. This observed oxide reduction can be attributed to the enhanced reducing effect of protein after self-assembly around droplets. During the self-assembly process, SPI can expose embedded hydrophobic residues with reductive effects, such as tyrosine and tryptophan,[48] making them more accessible to Ga. Thus, when sonicating Ga droplets in acetic acid aqueous solution with self-assembled SPI, oxide layers of Ga droplets are partially reduced. This enhanced reducing effect also contributes to maintaining Ga droplets in a less oxidized state.

Collectively, the enhanced electrical conductivity of the SPI-Ga composite films can be attributed to the synergetic attributes of protein self-assembly and the incorporation of Ga droplets. The self-assembled SPI reduces Ga oxide during sonication and protects Ga particles from further oxidation, as indicated by the XPS results (Figure 3d–g), attributing to higher electrical conductivity. Moreover, the self-assembly process around droplets is suggested to facilitate the protein's electron transfer ability,[49] as further elaborated in the next section. More importantly, the presence of Ga droplets, promoting Ga^{3+} ion release in acetic acid, infuses redox-active elements within self-assembled SPI, which also contributes to enhancing the electrical conductivity of the composite.[49]

2.3. Reaction of the SPI-Ga Films with Diatomic Gas Molecules

Proteins, such as heme protein, can selectively bind and recognize diatomic gases like CO.[50] Drawing inspiration from a heme-based carbon monoxide (CO) sensor,[51] we hypothesize that Ga droplets, with accessible redox-active surfaces[52] when coupled with self-assembled SPI, can serve as gas-reactive materials. To explore this potential, we assess the proof-of-concept gas-sensing performance of the SPI-Ga composite.

These gas sensors are fabricated by drop-casting the sonicated SPI solution and SPI/Ga solution onto an interdigitated transducer comprising silver–palladium (Ag–Pd) electrodes imprinted on alumina substrates (dimensions of electrodes are present in Figure S26, Supporting Information). SPI simply dissolved in acetic acid solution are labeled as native SPI, while those that denature under sonication and then self-assemble into nanofibrils are termed self-assembled SPI.[26a] Various SPI-related gas sensors are then subjected to preset CO of different concentrations in air ambience at room temperature (22 °C) with controlled humidity (70%) created by N_2, and the changes in electrical conductivity are recorded.

Figure 4a illustrates the response of a sample with only Ga droplets to CO gas, where exposure to CO reduces the resistance of the sensor. However, the resistance cannot recover to the original baseline, and the process is irreversible. CO reduces the Ga oxide layers irreversibly and more exposure to CO makes the sample further conductive in a permanent manner. As such, a sample with only Ga droplets cannot function as a real gas

© 2024 The Author(s). Advanced Functional Materials published by Wiley-VCH GmbH

16163028, 2024, 45, Downloaded from https://advanced.onlinelibrary.wiley.com/doi/10.1002/adfm.202405918 by University Of Southampton, Wiley Online Library on [23/07/2025]. See the Terms and Conditions (https://onlinelibrary.wiley.com/terms-and-conditions) on Wiley Online Library for rules of use; OA articles are governed by the applicable Creative Commons License

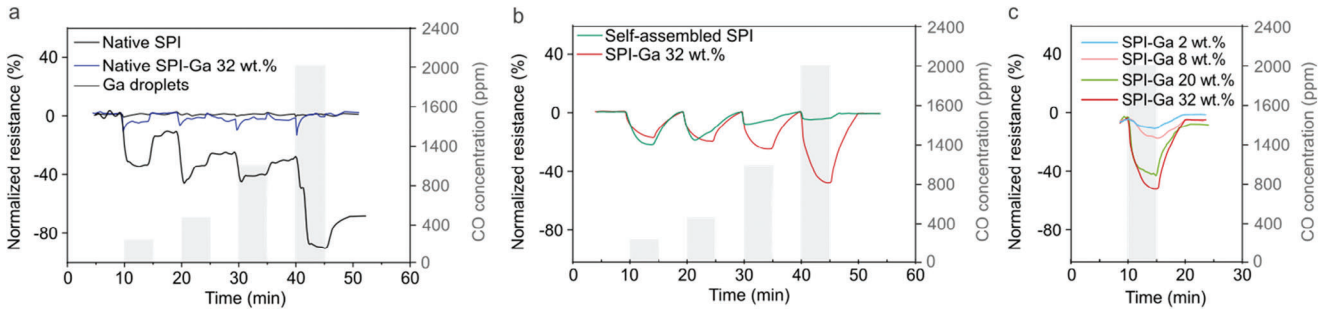

Figure 4. CO gas sensing properties of the SPI-Ga composite. a) Normalized electrical resistance change of Ga droplets, native SPI; native SPI-Ga 32 wt%; b) Self-assembled SPI and SPI-Ga 32 wt%; c) SPI-Ga composite with 2, 8, 20, and 32 wt% Ga concentration. All the figures are with CO gas input concentration profile.

sensor. Moreover, the electrical conductivity of native protein without self-assembly remains largely unchanged under CO exposure (Figure 4a). When Ga droplets are embedded in the native protein (native SPI-Ga 32 wt%), the resistance of the mixture displays a relatively sharp, rapid decrease in response to the CO gas, followed by a partial recovery (Figure 4a). However, the mixture behaves similarly in response to different CO concentrations, which is not ideal for gas sensing. In contrast, self-assembled SPI seem to sense the CO gas, while the responsiveness gradually declines over time (Figure 4b). Notably, when Ga droplets are encapsulated in self-assembled SPI (SPI-Ga 32 wt% sample), the electrical resistance of the composite material gradually decreases and recovers in agreement with CO gas flow. The intensity of resistance is closely correlated with the cyclical CO gas concentration variations (Figure 4b), suggesting enhanced CO sensing capability.

We then investigate the effect of different concentrations of Ga in the composites on CO gas sensing. With the increase of Ga droplets, the response of the composite becomes more proportional to the concentration of CO (Figure 4c). Self-assembled SPI with 32 wt% Ga performs the best compared to other concentrations. To show selectivity to CO, the self-assembled SPI with 32 wt% Ga is exposed to hydrogen gas (H_2), which like CO is also a reducing gas. In this case, SPI-Ga composite shows no response to 2% H_2 (Figure S27, Supporting Information – H_2 was tested in the same background environment condition as CO), which illustrates the plausibility of the selectivity of the films to diatomic gas molecules.

The difference in CO responses between the native SPI and the self-assembled SPI can be associated with the possibility that self-assembled SPI enhances electron transport capabilities, which is often associated with specific structural orders in organic materials.[49] Self-assembly aligns aromatic constituents, such as phenylalanine, tyrosine, and tryptophan, characterized by their delocalized electron systems that can engage in π-π interactions.[53] In this case, both stabilize the tertiary structure of the protein and also facilitates electron delocalization across aromatic rings.[49] However, the response of self-assembled SPI alone to CO is still irreversible. When incorporated with Ga droplets, the Ga droplets may provide redox-active surfaces, working similarly to the active center for natural gas sensor proteins such as iron-sulfur cluster and non-heme iron.[54] The merged conductive pathways formed by less oxidized Ga droplets further enhance such electron transfer ability along the self-assembled SPI nanofibrils. Therefore, the gas sensing ability and stability of self-assembled SPI are improved with incorporated Ga droplets.

2.4. Antibacterial Activity of Electrically-Stimulated SPI-Ga Films

Protein nanofibrils can be used for a variety of biocompatible coatings, specifically for cell scaffolds, wound healing, and tissue regeneration.[55] However, they face the challenge of bacterial adhesion, which leads to the formation of biofilms and impedes their long-term use.[56] Electrical stimulation has been shown to promote antibacterial activity.[57] Logically, incorporating antibacterial and conductive capabilities into films made of protein nanofibrils is advantageous for addressing this challenge. Given that Ga is considered a biocompatible metal with antibacterial[58] and electrical conductivity properties,[2a] we test our SPI-Ga films for antibacterial activity in an assisted electrical stimulation process.

The antibacterial activities of SPI-Ga films with different Ga concentrations are investigated on Escherichia coli (*E. coli*) K-12 after co-culturing for 48 h. The reduction of the bacteria cells is assessed through colony-forming unit (CFU) evaluation. The results show a positive correlation between Ga droplet concentration and antibacterial efficacy (Figure S28, Supporting Information). This enhancement in antibacterial activity is attributed to the increased release of Ga ions into the solution, which disrupts bacterial antioxidant enzymes via the "Trojan horse" mechanism in iron metabolism.[58,59] Thus, SPI-Ga 32 wt% is selected for the following experiment.

The experiment setup for the antibacterial testing is shown in **Figure 5a**. Before the antibacterial measurement with and without electrical-stimulation, the electrical properties of the SPI-Ga 32 wt% films are assessed in the M9 minimal medium (M9). The current/voltage (I/V) curves in Figure 5b reveal significant differences between the SPI film and the SPI-Ga 32 wt% film due to the addition of Ga. The SPI film exhibits non-conductive behavior in the M9 bacteria culture medium, while the SPI-Ga 32 wt% film shows electrical conductivity. Additionally, the open circuit potential of the SPI-Ga 32 wt% film is reduced compared to the SPI film (Figure 5c), indicating the influence of Ga and suggesting a more electrically stable surface.

Based on these results, the SPI-Ga 32 wt% film presents an electrically conductive interface in the bacteria culture medium,

© 2024 The Author(s). Advanced Functional Materials published by Wiley-VCH GmbH

16163028, 2024, 45, Downloaded from https://advanced.onlinelibrary.wiley.com/doi/10.1002/adfm.202405918 by University Of Southampton, Wiley Online Library on [23/07/2025]. See the Terms and Conditions (https://onlinelibrary.wiley.com/terms-and-conditions) on Wiley Online Library for rules of use; OA articles are governed by the applicable Creative Commons License

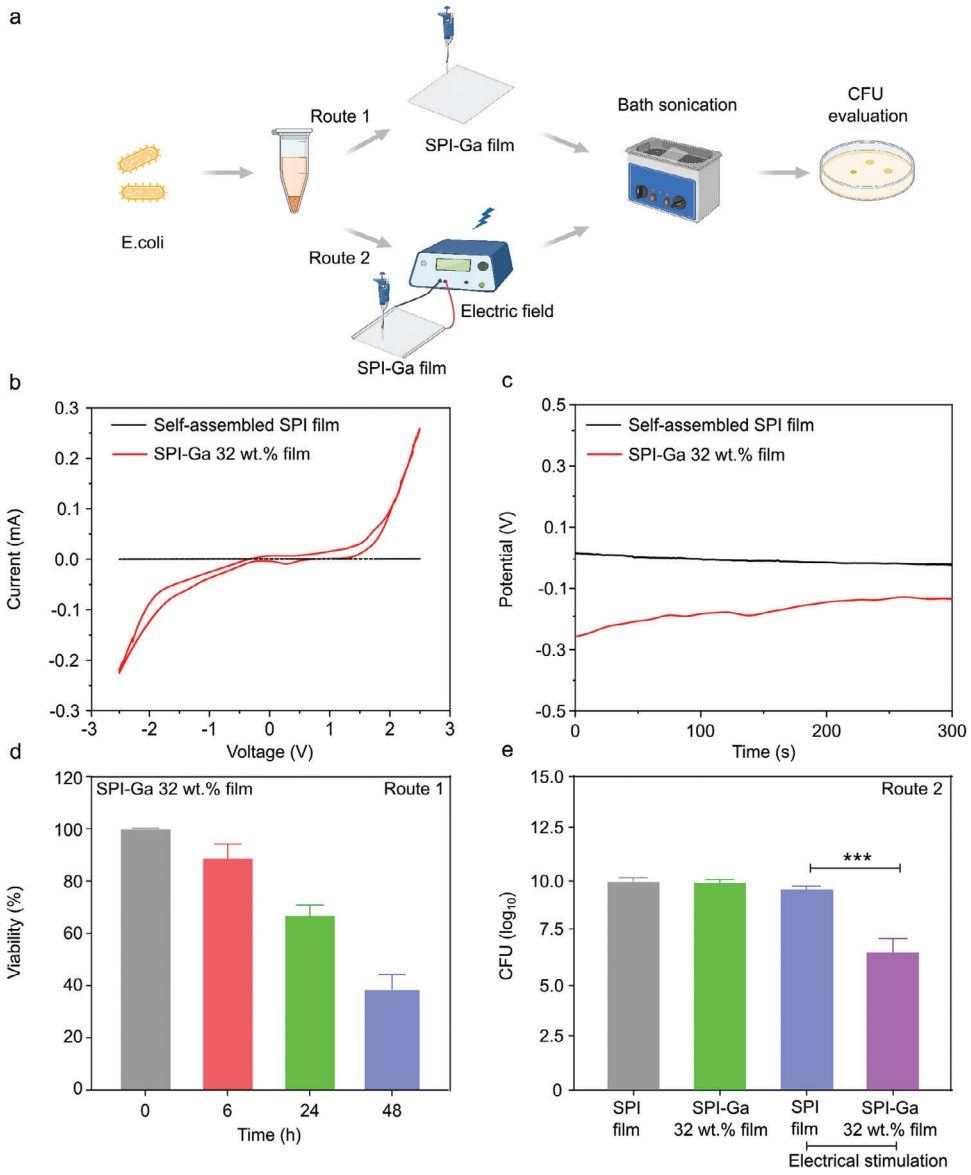

Figure 5. Antibacterial properties of the SPI-Ga composite films with electrical stimulation. a) Schematics of antibacterial test experiment setup and procedures. b) Cyclic voltammetry and c) Open circuit potential of SPI film and SPI-Ga 32 wt% film in M9 bacteria culture medium. d) The CFU reduction for *E. coli* K-12 of SPI-Ga 32 wt% film for 0, 6, 24, and 48 h. e) The CFU reduction for *E. coli* K-12 of SPI film and SPI-Ga 32 wt% film with and without electrical stimulation ($n = 4$, $^{***}p < 0.001$).

which can be assessed as a platform for electrical stimulation anti-bacterial experiments. First, the SPI-Ga film without electrical stimulation is assessed. After culturing with SPI-Ga 32 wt% film (1 cm^2) for 6, 24, and 48 h, a reduction in bacterial cells is observed compared to the SPI film, indicating the antibacterial effect of Ga (Figure 5d). Electrical stimulation for 1 h is applied to the film with bacteria. The voltage of 1 V is chosen to generate minimal water splitting, as seen in the *I/V* curves (Figure 5b). As shown in Figure 5e, the SPI film does not exhibit any bacterial activity, whereas the electrical stimulation exerts a limited inhibitory effect on *E. coli* K-12. In contrast, the addition of Ga droplets with electrical stimulation proves much more effective against *E. coli* K-12, resulting in a 2.53-log10 reduction in CFU compared to the untreated control group, killing > 99% of bacterial cells. The concentration of Ga ions in the bacterial solution before and after electrical stimulation, analyzed by inductively coupled plasma mass spectrometry (ICP-MS) (Figure S29, Supporting Information), reveals a nearly doubled release of Ga^{3+} ions from 12.68 to 24.76 mg L^{-1} due to electrical-induced oxidation. The induced current when voltage is applied also contributed to the enhanced antibacterial capabilities.[60] Overall, these enhanced antibacterial capabilities, especially under electrical stimulation, position SPI-Ga film as a viable medium for advanced biomedical applications.

© 2024 The Author(s). Advanced Functional Materials published by Wiley-VCH GmbH

16163028, 2024, 45, Downloaded from https://advanced.onlinelibrary.wiley.com/doi/10.1002/adfm.202405918 by University Of Southampton, Wiley Online Library on [23/07/2025]. See the Terms and Conditions (https://onlinelibrary.wiley.com/terms-and-conditions) on Wiley Online Library for rules of use; OA articles are governed by the applicable Creative Commons License

3. Conclusion and Discussion

We developed a composite film using Ga droplets and nanofibrils and investigated the electrical conductivity, mechanical properties, gas sensing properties, and antibacterial characteristics. By dispersing the Ga droplets into the pre-unfolded and denatured protein solution, self-assembled nanofibrils formed alongside the Ga droplets, contributing to the formation of a self-standing composite film. The synergetic attributes of nanofibrils and Ga droplets turned the non-conducive organic film into a conductive organic-inorganic hybrid composite. We found that nanofibrils, containing reductive motifs, decrease the oxidation of the Ga droplets, sintering Ga droplets. At the same time, the inclusion of Ga droplets within a certain concentration did not influence the form of the β-sheets rich nanofibrils in the composite, endowing the film with continuity and mechanical properties to maintain the structural integrity and consistent performance for both gas sensing and antibacterial applications. The SPI-Ga 32 wt% film with high electrical conductivity and well-structured nanofibrils were investigated in applications. The tuned electrical conductivity of the composite contributed to enhanced performance for selective sensing of CO, a diatomic molecule. While only Ga droplets exposure to CO changed the baseline during measurements and the response of bare SPI was unsatisfactory, the SPI-Ga composite exhibited a reversible response to different CO gas concentrations. Compared with other sensor materials for gas sensing,[61] these SPI-Ga composites exhibited several advantages including ease of preparation, operation at room temperature, and adjustable bias point by changing the Ga concentrations. Additionally, we also observed an augmented electrical stimulated antibacterial effect for SPI-Ga films. The composite films under electro-stimulation showed great potential for biomedical applications, such as wound healing, by reducing the bacterial growth propensity. Overall, this study introduced innovative possibilities for leveraging LMs with nanofibrils to develop functional materials and provided fundamental insights into the interaction between LM entities and proteins.

4. Experimental Section

Materials: Ga (beads, 99.999%) was purchased from Rotometals, USA. SPI (purity >90%) was kindly donated by a company, which could not be disclosed for contractual reasons. Acetic Acid Glacial AR (analytical grade) and glycerol (laboratory grade) were obtained from Chem-Supply Pty Ltd., Australia. Gold wires (Au, 0.25 mm diameter) were sourced from Sigma-Aldrich, Australia.

Preparation of Ga Droplets: Ga droplets were synthesized in a one-step procedure. In a typical procedure, Ga (300 mg) was dispersed in absolute ethanol (15 mL). The mixture was preheated at 50 °C for 5 min to melt Ga into a liquid state, followed by probe sonication (SONICS VCX 750) at 35% amplitude in burst mode (7 s on, 3 s off) for 30 or 60 min, with ice cooling. The resulting Ga droplets in ethanol were used within 3 days.

Preparation of SPI-Ga Films: To prepare the composite material, SPI (500 mg) was dispersed in acetic acid aqueous solution (8 mL, 30% v/v). The mixture underwent agitation until it achieved a turbid and highly viscous state. Subsequently, the mixture underwent sonication for 30 min with a 30% amplitude, utilizing pulse durations of 7 s on and 3 s off, without active cooling control. Ga droplets were separated through centrifugation, and the ethanol was substituted with acetic acid solutions (1 mL 30% v/v). Different concentrations of Ga particle solution were introduced and sonicated for an additional 3 min. Following sonication, glycerol (125 mg) was added as a plasticizer. The resultant hot solution was promptly poured into a preheated 7 cm petri dish at 90 °C and left to air dry for a minimum of 3 days at room temperature (19–22 °C) under typical ambient humidity levels (40–50% RH). The resulting dried film was then carefully detached from the petri dish and stored at room temperature for future applications.

Characterization: SEM and EDS were performed using an analytical SEM system (JEOL JSM-IT 500 HR with EDS, Bruker Silicon). For SPI and SPI-Ga hydrogel, they were the first solvents exchanged to ethanol with nice steps by immersing in 30, 50, 70, 80, 90, 95, 100, 100, and 100 vol% ethanol baths for 30 s under a Microwave processing system (PELCO BioWave Pro+, TED PELLA), respectively. Subsequently, the gels were dried by supercritical CO_2 according to the previously developed protocol.[62] Samples were coated with 15 nm platinum using a Leica ACE600 sputter coater.

Here XPS analysis was carried out using high-resolution XPS (ESCALAB250Xi, Thermo Scientific) with a monochromatic Al K α soft X-ray source (486.68 eV), operating at 120 W (13.8 kV × 8.7 mA), featuring a spot size of 500 µm and a photoelectron take-off angle of 90°. All XPS data were processed using the Advantage software and calibrated based on the C 1s peak at 284.8 eV. XRD patterns were collected using an MPD Xpert Multipurpose XRD system. Data was normalized based on the protein concentration in each sample. FTIR spectroscopy analyses were performed using a Spotlight 400 FTIR spectrometer in the UATR mode, covering the range of 1800−1400 cm^{-1}. UV−Vis transmittance spectra within the wavelength range of 200 to 800 nm were obtained with an ultraviolet−visible spectrometer (Agilent Cary 5000) featuring baseline correction.

For observing the protein self-assembly process, three samples were prepared from the 10 w/v% SPI solution post-sonication: prior to cooling, during cooling, and post-cooling. The details were as follows: for imaging proteins before self-assembly, a dilution step was conducted immediately after sonication using a pre-heated 30 v/v% acetic acid solution to achieve a concentration of 0.1 w/v%, and the solution was immediately deposited onto the TEM grids to prevent protein self-assembly. To image the nanofibril growth process, the sonicated protein solution during and after cooling was diluted in 30 v/v% acetic acid to a protein concentration of 0.1 w/v%. For observing the interaction between nanofibrils and Ga droplets, SPI-Ga 32 wt% was prepared. The sonicated SPI-Ga solution after cooling was diluted in 30 v/v% acetic acid to a protein concentration of 0.1 w/v% and deposited onto TEM grids. All samples were then stained with 2% uranyl acetate for 1 min. TEM, STEM, and STEM-EDX analyses were conducted using a JEOL JEM-F200, operating at 200 kV with a cold field-emission gun. The instrument was equipped with an annular dark-field detector and a JEOL windowless 100 mm^2 silicon drift x-ray detector.

Assessment of Interfacial Interaction of Ga and Protein: To obtain a dispersed nanofibrils solution, an SPI solution (10 w/v %) in acetic acid (30 v/v %) was prepared through sonication and immediately diluted to 5 w/v% to avoid gelation. After the temperature decreased to room temperature, Ga droplets (0.5 mg mL^{-1}) were incubated in the nanofibrils solution for 30 min at room temperature. Separately, another group of Ga droplets (0.5 mg mL^{-1}) was incubated with 5 w/v % SPI solution in 30% acetic acids without sonication for 30 min. Then the droplets were washed with DI water twice and suspended in DI water for measurement of the size and ζ-potential by Zetasizer Ultra (Malvern Instruments Ltd., UK). All measurements were performed at room temperature. Additionally, the wetting behavior of Ga droplets with nanofibrils was characterized by measuring the contact angle of Ga droplets on nanofibrils-coated glass slides. Nanofibrils could be coated on different substrates to form a thin film due to its solution-gel transition upon cooling.[26a] By gradually withdrawing the glass slides from the heated SPI nanofibrils solution and subsequent air drying at room temperature, the coating of SPI nanofibrils on the glass slides' surface was achieved. Unmodified glass slides served as the control group. To make the condition consistent with the SPI-Ga composite synthesis, the contact angles of Ga droplets with nanofibrils were measured in air and 30% acetic acid.

Circular Dichroism (CD) Spectra of SPI and SPI-Ga Composite: CD spectra of SPI and SPI-Ga samples were recorded on a Jasco J-800 series CD spectrometer at 25 °C. The measurements used a 1.0 nm bandwidth, 0.1 nm step interval, 50 nm min^{-1} scanning speed, 0.1 nm resolution,

© 2024 The Author(s). Advanced Functional Materials published by Wiley-VCH GmbH

16163028, 2024, 45, Downloaded from https://advanced.onlinelibrary.wiley.com/doi/10.1002/adfm.202405918 by University Of Southampton, Wiley Online Library on [23/07/2025]. See the Terms and Conditions (https://onlinelibrary.wiley.com/terms-and-conditions) on Wiley Online Library for rules of use; OA articles are governed by the applicable Creative Commons License

and 2 s average time. Far-UV spectra (190–260 nm) were obtained with a 0.1 cm quartz cell, averaging three scans per duplicate sample, and subtracting control scans of 0.15% acetic acid. SPI (2 w/v%) and SPI-Ga samples, both sonicated and diluted to 0.1 mg ml^{-1} in 0.15% acetic acid, were analyzed. The secondary structure contents were estimated from the CD spectra using BeStSel.

1-H Solid-State NMR: The samples for NMR included native SPI, self-assembled SPI, and SPI-Ga at 32 wt%. The self-assembled SPI and SPI-Ga 32 wt% samples were prepared using the supercritical CO_2 drying method applied to SPI and SPI-Ga hydrogel. The detailed protocol was described in the SEM sample preparation section. After drying, these samples were ground into powder. The 1H solid-state NMR measurements were rung on a Bruker Avance III, 300 instrument, with a 7 Tesla wide bore superconducting magnet, operating at a frequency of 300 MHz for the 1H nucleus. Approximately 15 mg of sample was center packed into a 4 mm zirconia rotor fitted with a Kel-f cap and spun to 12 kHz at the magic angle (MAS) in a wide-bore 4 mm HX NMR probe head. Faster spinning was not feasible as the rotation of the conductive Ga metal could result in excessive sample heating due to the magnetic breaking effect. This effect was of particular concern due to the low melting point of Ga, which would destabilize the spinning if molten. The 1H spectra were acquired with a single pulse as well as a Hahn echo pulse scheme using a 90° pulse width of 3.35 µs, a relaxation delay of 5 s to ensure full equilibration of the NMR signal, and up to 64 scans for sufficient signal to noise. The 1H chemical shifts were referenced using the 1H signal of adamantane at 1.78 ppm as a secondary reference.

Electrochemical Measurement: A CHI650E electrochemical station with a three-electrode cell setup was utilized. The working electrode was composed of the SPI film or SPI-Ga film. The reference electrode was a saturated calomel electrode, and the counter electrode consisted of gold. Gold wires were employed for electrical connections with the SPI film or SPI-Ga film. The chosen electrolyte was M9 minimal medium comprising Na_2HPO_4 (48 mM), KH_2PO_4 (22 mM), NaCl (9 mM), and NH_4Cl (19 mM), freshly supplemented with $MgSO_4$ (2 mM), $CaCl_2$ (100 µm), and glucose (20 mM). Cyclic voltammetry was performed over a potential range from −2.5 V to 2.5 V at a scan rate of 100 mV s^{-1} and a sensitivity of 1 µA V^{-1}. Additionally, open circuit potential measurements were taken at a scan rate of 100 mV s^{-1}, with a sensitivity of 0.10 A V^{-1}.

Thermal and Electrical Properties Measurement: TGA was carried out using a thermogravimetric analyzer (Q5000, TA Instruments) in a nitrogen environment to avoid combustion and oxidative degradation and in air for comparison. The analyses were conducted at a heating rate of 10 °C min^{-1}, reaching a final temperature of 700 °C. Before TGA analyses, the samples were pre-dried overnight in a vacuum oven set at 60 °C. A TA Discovery instrument (DSC250) was utilized for the DSC measurements, with temperatures ranging from −70 to 350 °C at 10 °C min^{-1} heating and cooling rates. The measurements were performed in the N_2 atmosphere. For electrical resistance measurement, the samples were cut into 1 cm x 1 cm strips and then assessed using a Siglent SDM3065X multimeter.

Tensile Test: Tensile testing was conducted using a Mark-10 ESM 303 instrument equipped with a 100 N load cell. The film specimens were prepared by cutting them into strips measuring 0.5 cm in width with a gauge length of 2 cm and were attached to paper frames. The edges of the frames were cut open before testing. The thickness of each film sample was measured using a microscope. The tensile tests were carried out at a loading speed of 2 mm min^{-1}. To ensure reliability, all tests were repeated a minimum of three times.

Gas Sensing Experiment: Solutions of the SPI film and SPI-Ga film (10 µL) were drop-cast onto Ag-Pd electrodes to form gas sensor assemblies. The experimental procedures were conducted within a LINKAM gas chamber (Linkam HFS600W-PB4), which underwent purging with high-purity nitrogen gas or synthetic air to establish a pristine baseline before each test. The target gas, carbon monoxide (CO), was introduced into the chamber at predetermined concentrations, regulated by three-channel mass flow controllers (MKSGE50A). Gas flow control and data acquisition were automated using LabVIEW software. Humidity within the chamber was maintained at 70% using a bubbler to provide a consistently high humidity environment which positivity affected the resistance of the self-assembled SPI (≈10 MΩ), whereas the nanofibril's resistance was greater than 40 MΩ at a 50% humidity level. The sensing signal, denoted as the impedance change of the sensor upon exposure to the target gas, was recorded using a two-probe configuration. The resistance signal was collected by applying an alternating current (AC) signal with an amplitude of 50 mV and a frequency of 20 Hz, with zero direct current (DC) bias. These electrical measurements were performed using a Wayne Kerr 6500B Impedance Analyzer.

Antibacterial Test: In this study, the antimicrobial SPI-Ga film was assessed for its effectiveness against negative Escherichia coli strain K-12 (ATCC 10 798) biofilm. A bacterial suspension with a concentration of $\approx 1 \times 10^7$ cells mL^{-1} was prepared by diluting an overnight culture at a 1:200 ratio in an M9 minimal medium. This medium was freshly supplemented with $MgSO_4$, $CaCl_2$, and glucose. Biofilm cultivation involved incubating bacterial suspension (1 mL) in tissue-culture treated 24-well plates for 6 h at 37 °C and 180 rpm. Subsequently, the culture was diluted 1:200 in phosphate-buffered saline (PBS), and the diluted bacterial solution (2 mL) was gently dispensed onto the SPI-Ga films placed in a 6-well microplate (Costar, Corning). A negative control with bacterial suspension (2 mL) was also included on the SPI film. After different durations (6, 24, and 48 h) of incubation at 37 °C, the films were removed from the wells and washed with PBS to remove loosely attached bacteria. The washed films were then placed into fresh PBS and subjected to 20 min of bath sonication (150 W, 40 kHz; Unisonics) to detach and homogenize the bacteria.[63] The viability of the detached bacteria was assessed through a drop plate method. CFU analysis was performed following incubation on Luria Bertani agar for 24 h at 37 °C. This experiment was carried out with two replicates and repeated in two independent trials. The concentrations of Ga metallic elements in the bacteria culture media were quantified using inductively coupled plasma mass spectrometry (ICP-MS, PerkinElmer, USA). Samples were digested in 1 M hydrogen chloride (HCl) before analysis.

Statistical Analysis: Data reported as mean ± SEM (standard error of the mean) were from at least three independent runs carried out at different times unless specified otherwise. Data analysis was performed by a one-way analysis of variance (ANOVA) to assess significance via GraphPad Prism 10 software. A P value of less than 0.05 was considered statistically significant.

Supporting Information

Supporting Information is available from the Wiley Online Library or from the author.

Acknowledgements

The authors acknowledge the facilities and the scientific and technical assistance of Microscopy Australia at the Electron Microscope Unit (EMU) within the Mark Wainwright Analytical Centre (MWAC) at UNSW Sydney. The authors thank Joanna Richmond for assistance and advice with SEM sample preparation and Zeno Rizqi Ramadhan for TEM imaging. The authors thank Michelle Wood for assistance and advice with FTIR that was carried out at Sydney Analytical, a core research facility at the University of Sydney. The authors thank Hao Luo at UNSW Sydney for assistance with antibacterial tests. The authors thank Zhenbang (Charlie) Cao for assistance and advice with sonication and zeta potential measurement. This work was supported by the Australian Research Council (ARC) Laureate Fellowship grant (FL180100053), ARC Discovery Project grant (DP230102813), and DECRA fellowship (DE230100837).

Open access publishing facilitated by University of New South Wales, as part of the Wiley - University of New South Wales agreement via the Council of Australian University Librarians.

Conflict of Interest

The authors declare no conflict of interest.

© 2024 The Author(s). Advanced Functional Materials published by Wiley-VCH GmbH

16163028, 2024, 45, Downloaded from https://advanced.onlinelibrary.wiley.com/doi/10.1002/adfm.202405918 by University Of Southampton, Wiley Online Library on [23/07/2025]. See the Terms and Conditions (https://onlinelibrary.wiley.com/terms-and-conditions) on Wiley Online Library for rules of use; OA articles are governed by the applicable Creative Commons License

Author Contributions

Y.S. and K.K.Z. conceived the idea. L.L. conducted the experiments and characterizations and analyzed the data with the help of J.Z., C.W., M.B., S.C., J.I., L.S., M.M., T.L.S., C.Z., J.T., E.H.H.W., J.Z. M.R. provided many suggestions on the experiment design and figures. M.K. assisted in the gas sensing test, Y.H. assisted in the tensile test, and Z.S. and H.L. assisted in the antibacterial tests. A.R. assisted in the solid 1H NMR test. Y.S., K.K.-Z., and F.M.A. supervised the research project, interpreted the results, and revised the paper. The first manuscript was drafted by L.L., K.K.-Z., Y.S., and F.-M.A. with input from all the authors.

Data Availability Statement

The data that support the findings of this study are available from the corresponding author upon reasonable request.

Keywords

antibacterial properties, CO sensing, liquid metal, nanofibrils, self-assembly

Received: April 7, 2024
Revised: August 9, 2024
Published online: August 30, 2024

[1] A. Zavabeti, T. Daeneke, A. F. Chrimes, A. P. O'Mullane, J. Zhen Ou, A. Mitchell, K. Khoshmanesh, K. Kalantar-zadeh, *Nat. Commun.* **2016**, *7*, 12402.
[2] a) S.-Y. Tang, C. Tabor, K. Kalantar-Zadeh, M. D. Dickey, *Annu. Rev. Mater. Res.* **2021**, *51*, 381; b) D. Wang, J. Ye, Y. Bai, F. Yang, J. Zhang, W. Rao, J. Liu, *Adv. Mater.* **2023**, *35*, 2303533; c) S. Chen, H.-Z. Wang, R.-Q. Zhao, W. Rao, J. Liu, *Matter.* **2020**, *2*, 1446; d) N. Yang, F. Gong, Y. Zhou, Q. Yu, L. Cheng, *Coord. Chem. Rev.* **2022**, *471*, 214731.
[3] a) K. Zuraiqi, A. Zavabeti, F.-M. Allioux, J. Tang, C. K. Nguyen, P. Tafazolymotie, M. Mayyas, A. V. Ramarao, M. Spencer, K. Shah, C. F. McConville, K. Kalantar-Zadeh, K. Chiang, T. Daeneke, *Joule.* **2020**, *4*, 2290; b) M. A. Rahim, J. Tang, A. J. Christofferson, P. V. Kumar, N. Meftahi, F. Centurion, Z. Cao, J. Tang, M. Baharfar, M. Mayyas, F.-M. Allioux, P. Koshy, T. Daeneke, C. F. McConville, R. B. Kaner, S. P. Russo, K. Kalantar-Zadeh, *Nat. Chem.* **2022**, *14*, 935.
[4] M. Baharfar, K. Kalantar-Zadeh, *ACS Sens.* **2022**, *7*, 386.
[5] M. D. Dickey, *Adv. Mater.* **2017**, *29*, 1606425.
[6] a) S.-Y. Tang, R. Qiao, *Acc. Mater. Res.* **2021**, *2*, 966; b) S. Chen, R. Zhao, X. Sun, H. Wang, L. Li, J. Liu, *Adv. Healthcare Mater.* **2023**, *12*, 2201924.
[7] X. Zhao, M. Qiao, Y. Zhou, J. Liu, *Droplet.* **2024**, *3*, 104.
[8] L. Ren, X. Xu, Y. Du, K. Kalantar-Zadeh, S. X. Dou, *Mater. Today.* **2020**, *34*, 92.
[9] M. Zhang, S. Yao, W. Rao, J. Liu, *Mater. Sci. Eng. R Rep.* **2019**, *138*, 1.
[10] W. Xie, F.-M. Allioux, J. Z. Ou, E. Miyako, S.-Y. Tang, K. Kalantar-Zadeh, *Trends Biotechnol.* **2021**, *39*, 624.
[11] F.-M. Allioux, S. Merhebi, L. Liu, F. Centurion, R. Abbasi, C. Zhang, J. Ireland, J. M. Biazik, M. Mayyas, J. Yang, M. Mousavi, M. B. Ghasemian, J. Tang, W. Xie, M. Arifur Rahim, K. Kalantar-Zadeh, *J. Mater. Chem. B.* **2023**, *11*, 3941.
[12] J. Yang, W. Cheng, K. Kalantar-zadeh, *Proc. IEEE Inst. Electr. Electron Eng.* **2019**, *107*, 2168.
[13] a) S. A. Chechetka, Y. Yu, X. Zhen, M. Pramanik, K. Pu, E. Miyako, *Nat. Commun.* **2017**, *8*, 15432; b) Y. Lu, Q. Hu, Y. Lin, D. B. Pacardo, C. Wang, W. Sun, F. S. Ligler, M. D. Dickey, Z. Gu, *Nat. Commun.* **2015**, *6*, 10066.
[14] L. Wang, R. Lai, L. Zhang, M. Zeng, L. Fu, *Adv. Mater.* **2022**, *34*, 2201956.
[15] A. Rodrigo-Navarro, S. Sankaran, M. J. Dalby, A. del Campo, M. Salmeron-Sanchez, *Nat. Rev. Chem.* **2021**, *6*, 1175.
[16] X. Li, M. Li, J. Xu, J. You, Z. Yang, C. Li, *Nat. Commun.* **2019**, *10*, 3514.
[17] B. Chen, Y. Cao, Q. Li, Z. Yan, R. Liu, Y. Zhao, X. Zhang, M. Wu, Y. Qin, C. Sun, W. Yao, Z. Cao, P. M. Ajayan, M. O. L. Chee, P. Dong, Z. Li, J. Shen, M. Ye, *Nat. Commun.* **2022**, *13*, 1206.
[18] S. Ling, D. L. Kaplan, M. J. Buehler, *Nat. Rev. Chem.* **2018**, *3*, 18016.
[19] A. Quijano-Rubio, H.-W. Yeh, J. Park, H. Lee, R. A. Langan, S. E. Boyken, M. J. Lajoie, L. Cao, C. M. Chow, M. C. Miranda, J. Wi, H. J. Hong, L. Stewart, B.-H. Oh, D. Baker, *Nature.* **2021**, *591*, 482.
[20] F. Wang, W. Xia, M. Zhang, R. Wu, X. Song, Y. Hao, Y. Feng, L. Zhang, D. Li, W. Kang, C. Liu, L. Liu, *Chem. Sci.* **2023**, *14*, 10914.
[21] a) Y. Shen, A. Levin, A. Kamada, Z. Toprakcioglu, M. Rodriguez-Garcia, Y. Xu, T. P. J. Knowles, *ACS Nano.* **2021**, *15*, 5819; b) S. Ling, Q. Wang, D. Zhang, Y. Zhang, X. Mu, D. L. Kaplan, M. J. Buehler, *Adv. Funct. Mater.* **2018**, *28*, 1705291.
[22] G. Wei, Z. Su, N. P. Reynolds, P. Arosio, I. W. Hamley, E. Gazit, R. Mezzenga, *Chem. Soc. Rev.* **2017**, *46*, 4661.
[23] a) R. F. Banglmaier, E. A. Sander, P. J. VandeVord, *Acta Biomater.* **2015**, *17*, 26; b) S. Zhong, W. E. Teo, X. Zhu, R. W. Beuerman, S. Ramakrishna, L. Y. Yung, *J. Biomed. Mater. Res., Part A.* **2006**, *79*, 456.
[24] M. Díaz-Caballero, S. Navarro, S. Ventura, *Biomacromolecules.* **2021**, *22*, 2822.
[25] J. Dolai, A. Maity, B. Mukherjee, R. Ray, N. R. Jana, *ACS Appl. Mater. Interfaces.* **2024**, *16*, 217.
[26] a) A. Kamada, M. Rodriguez-Garcia, F. S. Ruggeri, Y. Shen, A. Levin, T. P. J. Knowles, *Nat. Commun.* **2021**, *12*, 3529; b) T. Li, J. Zhou, M. Peydayesh, Y. Yao, M. Bagnani, I. Kutzli, Z. Chen, L. Wang, R. Mezzenga, *Adv. Sustainable Syst.* **2023**, *7*, 2200414; c) D. Xu, J. Zhou, W. L. Soon, I. Kutzli, A. Molière, S. Diedrich, M. Radiom, S. Handschin, B. Li, L. Li, S. J. Sturla, C. Y. Ewald, R. Mezzenga, *Nat. Commun.* **2023**, *14*, 6806.
[27] G. Nyström, M. P. Fernández-Ronco, S. Bolisetty, M. Mazzotti, R. Mezzenga, *Adv. Mater.* **2016**, *28*, 472.
[28] M. B. Bryning, D. E. Milkie, M. F. Islam, L. A. Hough, J. M. Kikkawa, A. G. Yodh, *Adv. Mater.* **2007**, *19*, 661.
[29] H. Hu, Z. Zhao, W. Wan, Y. Gogotsi, J. Qiu, *Adv. Mater.* **2013**, *25*, 2219.
[30] G. Nyström, L. Roder, M. P. Fernández-Ronco, R. Mezzenga, *Adv. Funct. Mater.* **2018**, *28*, 1703609.
[31] a) S. Ling, Z. Qin, W. Huang, S. Cao, D. L. Kaplan, M. J. Buehler, *Sci. Adv.* **2017**, *3*, 1601939; b) Y. Yuan, N. Solin, *ACS Appl. Bio Mater.* **2022**, *5*, 3360; c) H. Sun, Z. Xu, C. Gao, *Adv. Mater.* **2013**, *25*, 2554.
[32] L. Zhou, Y. Peng, N. Zhang, R. Du, R. Hübner, X. Wen, D. Li, Y. Hu, A. Eychmüller, *Adv. Opt. Mater.* **2021**, *9*, 2100352.
[33] X. Wang, L. Fan, J. Zhang, X. Sun, H. Chang, B. Yuan, R. Guo, M. Duan, J. Liu, *Adv. Funct. Mater.* **2019**, *29*, 1907063.
[34] Y. Hou, P. Zhang, D. Wang, J. Liu, W. Rao, *ACS Appl. Mater. Interfaces.* **2020**, *12*, 27984.
[35] W. Gao, Y. Wang, Q. Wang, G. Ma, J. Liu, *J. Mater. Chem. B.* **2022**, *10*, 829.
[36] T. Li, J. Kambanis, T. L. Sorenson, M. Sunde, Y. Shen, *Biomacromolecules.* **2024**, *25*, 5.
[37] F. Song, D.-L. Tang, X.-L. Wang, Y.-Z. Wang, *Biomacromolecules.* **2011**, *12*, 3369.
[38] P. B. Stathopulos, G. A. Scholz, Y.-M. Hwang, J. A. O. Rumfeldt, J. R. Lepock, E. M. Meiering, *Protein Sci.* **2004**, *13*, 3017.
[39] a) H. Lee, G. Yildiz, L. C. dos Santos, S. Jiang, J. E. Andrade, N. J. Engeseth, H. Feng, *Food Hydrocolloid.* **2016**, *55*, 200; b) R. Pathak, S. K. Bhangu, G. J. O. Martin, F. Separovic, M. Ashokkumar, *Eur. Biophys. J.* **2022**, *51*, 335.
[40] Y. Wan, S. Guo, *Food Biophys.* **2019**, *14*, 164.

© 2024 The Author(s). Advanced Functional Materials published by Wiley-VCH GmbH

16163028, 2024, 45, Downloaded from https://advanced.onlinelibrary.wiley.com/doi/10.1002/adfm.202405918 by University Of Southampton, Wiley Online Library on [23/07/2025]. See the Terms and Conditions (https://onlinelibrary.wiley.com/terms-and-conditions) on Wiley Online Library for rules of use; OA articles are governed by the applicable Creative Commons License

[41] a) C. Zhang, F.-M. Allioux, M. A. Rahim, J. Han, J. Tang, M. B. Ghasemian, S.-Y. Tang, M. Mayyas, T. Daeneke, P. Le-Clech, R. B. Kaner, D. Esrafilzadeh, K. Kalantar-Zadeh, *Chem. Mater.* **2020**, *32*, 4808; b) Y. Gao, H. Xiao, X. Ma, Z. Yue, C. Liu, M. Zhao, L. Zhang, J. Zhang, E. Luo, T. Hu, B. Lv, J. Jia, H. Wu, *J. Mater. Chem. A.* **2024**, *12*, 8272.

[42] a) F. S. Ruggeri, G. Longo, S. Faggiano, E. Lipiec, A. Pastore, G. Dietler, *Nat. Commun.* **2015**, *6*, 7831; b) H. Yang, S. Yang, J. Kong, A. Dong, S. Yu, *Nat. Protoc.* **2015**, *10*, 382.

[43] X. Wang, D. V. M. Repaka, A. Suwardi, Q. Zhu, J. Wu, J. Xu, *Trans. Tianjin Univ.* **2023**, *29*, 209.

[44] M. Losurdo, A. Suvorova, S. Rubanov, K. Hingerl, A. S. Brown, *Nat. Mater.* **2016**, *15*, 995.

[45] K. Akyildiz, J.-H. Kim, J.-H. So, H.-J. Koo, *J. Ind. Eng. Chem.* **2022**, *116*, 120.

[46] a) Y. Xiao, Y. Liu, S. Kang, K. Wang, H. Xu, *Food Hydrocolloids.* **2020**, *106*, 105898; b) X. Liu, R. Song, W. Zhang, C. Qi, S. Zhang, J. Li, *Sci. Rep.* **2017**, *7*, 44289.

[47] a) Y. Wang, Y. Shen, G. Qi, Y. Li, X. S. Sun, D. Qiu, Y. Li, *Int. J. Biol. Macromol.* **2020**, *149*, 609; b) W. Surmacz-Chwedoruk, I. Malka, Ł. Bożycki, H. Nieznańska, W. Dzwolak, *PLoS One.* **2014**, *9*, 86320.

[48] a) Y. Shen, L. Posavec, S. Bolisetty, F. M. Hilty, G. Nyström, J. Kohlbrecher, M. Hilbe, A. Rossi, J. Baumgartner, M. B. Zimmermann, R. Mezzenga, *Nat. Nanotechnol.* **2017**, *12*, 642; b) P. Qin, T. Wang, Y. Luo, *J. Agric. Food Res.* **2022**, *7*, 100265; c) S. Si, T. K. Mandal, *Chem.-Eur. J.* **2007**, *13*, 3160.

[49] N. L. Ing, M. Y. El-Naggar, A. I. Hochbaum, *J. Phys. Chem. B.* **2018**, *122*, 10403.

[50] A. Sarkar, E. L. Carter, J. B. Harland, A. L. Speelman, N. Lehnert, S. W. Ragsdale, *Proc. Natl. Acad. Sci. USA.* **2021**, *118*, 2016717118.

[51] A. C. S. Gondim, W. G. Guimarães, E. H. S. Sousa, *BioChem.* **2022**, *2*, 43.

[52] T. Daeneke, K. Khoshmanesh, N. Mahmood, I. A. de Castro, D. Esrafilzadeh, S. J. Barrow, M. D. Dickey, K. Kalantar-zadeh, *Chem. Soc. Rev.* **2018**, *47*, 4073.

[53] R. Thakuria, N. K. Nath, B. K. Saha, *Cryst. Growth Des.* **2019**, *19*, 523.

[54] S. Aono, *Dalton Trans.* **2008**, *24*, 3137.

[55] K. G. DeFrates, R. Moore, J. Borgesi, G. Lin, T. Mulderig, V. Beachley, X. Hu, *Nanomaterials.* **2018**, *8*, 457.

[56] M. Katsikogianni, Y. F. Missirlis, *Eur. Cells Mater.* **2004**, *8*, 37.

[57] M. R. Asadi, G. Torkaman, *Adv. Wound Care.* **2014**, *3*, 91.

[58] L. Li, H. Chang, N. Yong, M. Li, Y. Hou, W. Rao, *J. Mater. Chem. B.* **2021**, *9*, 85.

[59] a) F. Li, F. Liu, K. Huang, S. Yang, *Front. Bioeng. Biotechnol.* **2022**, *10*, 827960; b) C. C. Qu, Y. T. Liang, X. Q. Wang, S. Gao, Z. Z. He, X. Y. Sun, *Bioengineering (Basel).* **2022**, *9*, 416.

[60] S. B. Rajendran, K. Challen, K. L. Wright, J. G. Hardy, *J. Funct. Biomater.* **2021**, *12*, 40.

[61] W. Zhou, P. Xiao, T. Chen, *Acc. Mater. Res.* **2023**, *4*, 334.

[62] Y. Shen, G. Nyström, R. Mezzenga, *Adv. Funct. Mater.* **2017**, *27*, 1700897.

[63] a) C. Rux, A. Wittmer, A. Stork, K. Vach, E. Hellwig, F. Cieplik, A. Al-Ahmad, *Clin. Oral Invest.* **2023**, *28*, 19; b) Z. Shao, K. Hakobyan, J. Xu, R. Chen, N. Kumar, M. Willcox, E. H. H. Wong, *ACS Appl. Polym. Mater.* **2023**, *5*, 8735.

© 2024 The Author(s). Advanced Functional Materials published by Wiley-VCH GmbH

16163028, 2024, 45, Downloaded from https://advanced.onlinelibrary.wiley.com/doi/10.1002/adfm.202405918 by University Of Southampton, Wiley Online Library on [23/07/2025]. See the Terms and Conditions (https://onlinelibrary.wiley.com/terms-and-conditions) on Wiley Online Library for rules of use; OA articles are governed by the applicable Creative Commons License